Wind and Structures, *Vol. 36, No. 2 (2023) 75-90*
https://doi.org/10.12989/was.2023.36.2.075

Wind-sand tunnel experiment on the windblown sand transport and sedimentation over a two-dimensional sinusoidal hill

Lorenzo Raffaele[*1,2,3], Gertjan Glabeke[2a] and Jeroen van Beeck[2b]

[1]*Department of Architecture and Design, Politecnico di Torino, Viale Mattioli 39, I-10125, Torino, Italy*
[2]*Environmental and Applied Fluid Dynamics Department, von Karman Institute for Fluid Dynamics, Waterloosesteenweg 72, B-1640, Sint-Genesius-Rode, Belgium*
[3]*Windblown Sand Modeling and Mitigation Joint Research Group, Italy-France*

(*Received July 29, 2022, Revised January 23, 2023, Accepted February 21, 2023*)

Abstract. Turbulent wind flow over hilly terrains has been extensively investigated in the scientific literature and main findings have been included in technical standards. In particular, turbulent wind flow over nominally two-dimensional hills is often adopted as a benchmark to investigate wind turbine siting, estimate wind loading, and dispersion of particles transported by the wind, such as atmospheric pollutants, wind-driven rain, windblown snow. Windblown sand transport affects human-built structures and natural ecosystems in sandy desert and coastal regions, such as transport infrastructures and coastal sand dunes. Windblown sand transport taking place around any kind of obstacle is rarely in equilibrium conditions. As a result, the modelling of windblown sand transport over complex orographies is fundamental, even if seldomly investigated. In this study, the authors present a wind-sand tunnel test campaign carried out on a nominally two-dimensional sinusoidal hill. A first test is carried out on a flat sand fetch without any obstacle to assess sand transport in open field conditions. Then, a second test is carried out on the hill model to assess the sand flux overcoming the hill and the morphodynamic evolution of the sand sedimenting over its upwind slope. Finally, obtained results are condensed into a dimensionless parameter describing its sedimentation capability and compared with values resulting from other nominally two-dimensional obstacles from the literature.

Keywords: complex orography; particle image velocimetry; particle tracking velocimetry; sinusoidal hill; wind tunnel; windblown sand

1. Introduction

Turbulent wind flow over hilly terrains has been extensively investigated in the scientific literature in order to define wind turbine siting (e.g., Porté-Agel *et al*. 2020), estimate wind loading on structures (e.g. Safaei Pirooz and Flay 2017), and predict atmospheric dispersion of particles transported by wind (e.g., Sun *et al*. 2012). In particular, turbulent wind flow over two-dimensional hill profiles is often adopted as a benchmark because of the non-trivial flow phenomena they induce despite their geometric simplicity (see e.g., *et al*. 2002, Bitsuamlak *et al*. 2004, 2006). On the upwind side, the incoming wind flow decelerates then accelerates along the hill upwind slope up to the top. On the downwind side, the flow may involve separation of the boundary layer depending on the hill steepness and aerodynamic roughness (Finnigan 1988, Cao and Tamura 2006, 2007). Finally, the reattachment of the boundary layer can occur along the downwind slope or far downstream mainly depending on Reynolds number, aerodynamic roughness and turbulence intensity.

The investigation of particles dispersion and deposition over complex orographies gained attention in the scientific literature (e.g., Parker and Kinnersley 2004). Existing studies employ both experimental and computational approaches by referring to nominally two-dimensional hills in order to investigate several kinds of two-phase transport, such as wind-driven rain (Blocken *et al*. 2005), windblown snow (Comola *et al*. 2019), and atmospheric dust transport (Goossens 2006). Among two-phase flows, the modelling of windblown sand transport over complex orographies is also worth of interest given its hazardous effect on both building environment and human activities (such as transport infrastructures, industrial facilities, buildings, urban areas, farms, see Bruno *et al*. 2018) and ecological systems (such as coastal dunes and desert oasis, see Sherman and Nordstrom 1994, Ke *et al*. 2020), in sandy coastal and desert environments. On the one hand, coastal infrastructures are experiencing the increased frequency of windstorms induced by climate change, giving rise to sand transport events from sandy coasts to urbanized areas (Strypsteen *et al*. 2020). On the other hand, desert regions increasingly host human activities and built infrastructures given the increasing number of projects currently ongoing or planned across North Africa, Middle East, and Southeast Asia (Raffaele and Bruno 2019, 2020).

Windblown sand transport occurs when the wind shear stress exerted by the wind on the sand surface is higher than the so-called threshold shear stress, mainly depending on the sand granulometry (Shao 2008). Transported sand grains

*Corresponding author, Ph.D. Assistant Professor
E-mail: lorenzo.raffaele@polito.it
[a]Ph.D. Student, Senior Test Engineer
[b]Ph.D. Professor

ISSN: 1226-6116 (Print), 1598-6225 (Online)

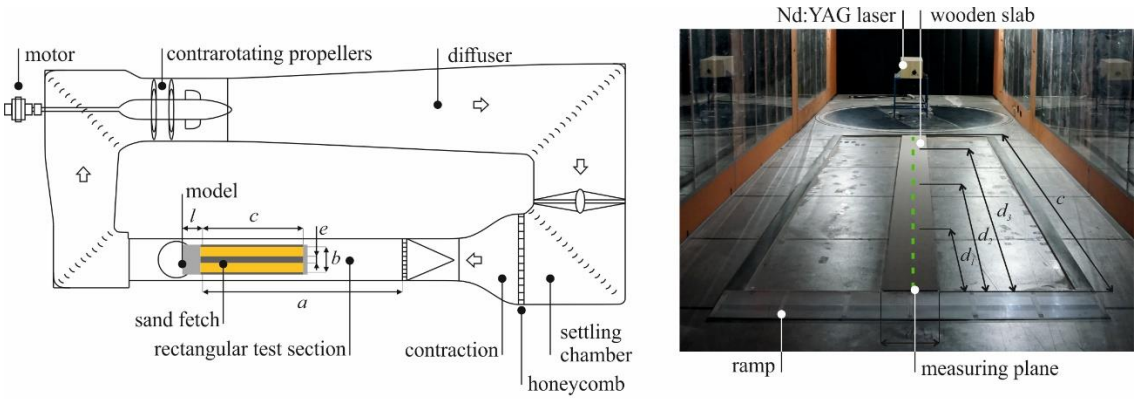

(a) (b)

Fig. 1 Plan view of the VKI L-1B wind tunnel (a) and wind tunnel test setup (Setup 0) to measure wind field (b)

follow a ballistic trajectory, eventually impacting on the sand bed and inducing new particles to detach from the surface. This phenomenon, known as saltation, develops close to the sand bed with a typical maximum saltation layer height of about 10-20 cm and it is the main mode of motion in terms of transported sand mass (Kok *et al*. 2012). Over flat sand bed and under uniform wind speed, sand transport progressively develops along the fetch distance eventually reaching equilibrium conditions, i.e., erosion and deposition are balanced (Andreotti *et al*. 2010). Conversely, sudden changes in the wind shear stress (induced by ground geometry, obstacles, or non-uniform wind conditions) result in non-equilibrium conditions, i.e., the amount of sand eroded/sedimented do not balance each other leading to the morphodynamic evolution of the sand bed (Preziosi *et al*. 2015). As a result, the modelling of windblown sand transport over complex orographies is fundamental to predict both sand flux and morphodynamic evolution of the sand bed under non-equilibrium conditions. In particular, sinusoidal-like hill profile is of particular interest being one of the many shapes attained by aeolian landforms throughout the evolution towards fully developed sand dunes (Claudin *et al*. 2013), by earthworks acting as sand mitigation measures (Phillips 2011), and being a typical geometry adopted for benchmarking purposes.

The modelling of windblown sand transport over complex orographies can be performed through physical experiments or computational simulations. Physical experiments usually translate into wind tunnel scale tests. Wind-sand tunnel testing allows to replicate in a controlled setup, and measure with high accuracy the spatial and temporal evolution of wind and sand state variables. However, wind-sand tunnel testing shows both replicability and measuring deficiencies. Replicability deficiencies are related to the inescapable similarity mismatching arising from the impossibility of jointly satisfying all multiphase/multiscale geometric and kinematic similarity requirements when scale models are tested (Raffaele *et al*. 2021), and the difficulty in the reproduction of in-equilibrium sand transport due to fetch effect (Dong *et al*. 2004). Measuring deficiencies are related to the technical difficulty of measuring the wind shear stress with simultaneous sand transport and the sand flux close to the wind-sand interface. The computational simulation of windblown sand flow allows to overcome the above wind-sand tunnel testing deficiencies. In particular, it is mainly carried out through the modelling of the wind flow through RANS or LES approaches, while the dispersed sand phase can be modeled through Lagrangian or Eulerian approaches (e.g., Lo Giudice *et al*. 2019). The computational simulation of windblown sand flow for engineering applications is primarily carried out through the resolution of RANS approach coupled with Eulerian or Lagrangian approaches for the solid phase (e.g., Tominaga *et al*. 2018, Lo Giudice and Preziosi 2020, Ma *et al*. 2021). However, computational simulations shall be carefully employed only after their validation on the basis of wind-sand tunnel measurements.

Despite its importance, sand transport over complex orographies, such as shallow or steep hills, is only slightly investigated in the literature. To the authors' best knowledge, the experimental studies of Farimani *et al*. (2011), Ferreira and Fino (2012), Simoëns *et al*. (2015), and the computational study of Huang *et al*. (2019) are the only remarkable exceptions. In particular, Farimani *et al*. (2011) and Ferreira and Fino (2012) investigate the morphodynamic evolution of a single and two consecutive two-dimensional erodible sinusoidal hills through wind-sand tunnel testing, while Simoëns *et al*. (2015) and Huang *et al*. (2019) investigate sand particles concentration and velocity profiles around a single and two consecutive two-dimensional non-erodible Gaussian hills through wind-sand tunnel testing and computational simulation. However, past studies (i) do not investigate the evolution over time of sand flux and simultaneous sand bed morphodynamics, and (ii) completely overlook dimensionless similarity parameters to reproduce sand erosion, transport and sedimentation around ground-mounted obstacles (see e.g., White 1996, Yu *et al*. 2019, Raffaele *et al*. 2021).

In the light of the above state of the art, the existing literature lacks of detailed measurements of windblown sand transport over hilly terrains enabling, on the one hand, the deep investigation of windblown sand flow features and, on the other hand, the calibration and validation of computational simulations through wind-sand tunnel measurements. The general goal of this study is to fill this

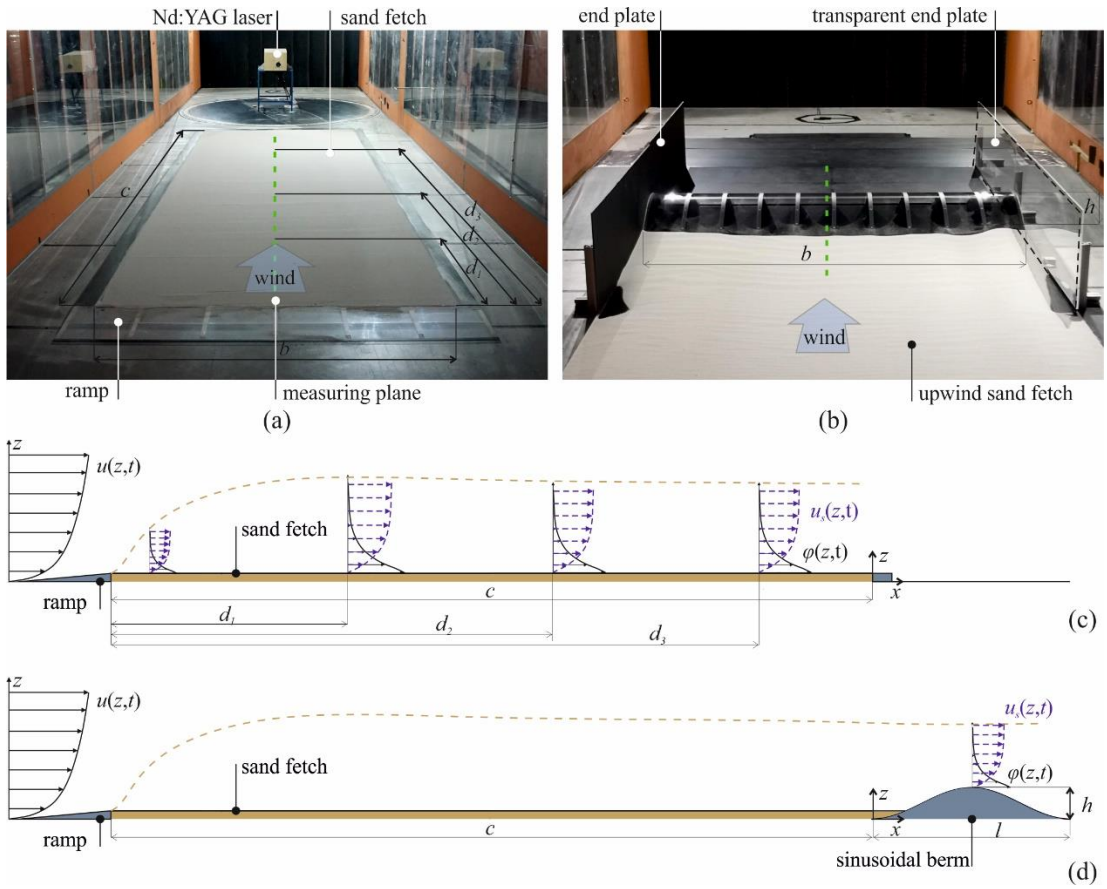

Fig. 2 Wind-sand tunnel test setup over flat sand fetch (Setup A, a) and sinusoidal hill (Setup B, b), and corresponding schemes of the measuring cross-sections (c, d)

gap of knowledge by critically analyzing a wind-sand tunnel test on a two-dimensional sinusoidal hill. In particular, the study is intended to (i) investigate the attainment of in-equilibrium conditions of incoming sand transport over flat sand fetch, (ii) investigate the variability in time and space of sand particle dispersion over the hill model, (iii) assess the time-varying morphodynamic evolution of the sedimented sand bed, and (iv) condense the results of engineering interest in terms of a dimensionless parameter synthesizing sedimentation capability.

The paper is organized into three further sections. In Sect. 2, the layout of the wind-sand tunnel test is introduced by outlining the adopted facility, setup and measuring equipment. In Sect. 3, results are presented and discussed. Finally, conclusions and perspectives are outlined in Sect. 4.

2. Layout of the wind-sand tunnel test

In the following, the wind tunnel facility is introduced, the adopted setup is described and justified through similarity requirements for the multiphase and multiscale wind-sand flow, and finally the measuring equipment is detailed.

2.1 Wind tunnel facility

The wind tunnel test is carried out in the wind tunnel L-1B of von Karman Institute for Fluid Dynamics. The facility is a closed-circuit wind tunnel with a test section length of about 20 m, and a cross-section of height h_{wt} = 2 m and width w_{wt} = 3 m (see Fig. 1(a)).

A typical open field low-roughness boundary layer for sand desert conditions is reproduced by placing a monoplane grid with a mesh size of 0.02×0.02 m at the inlet of the test section. A flat wooden slab of length c = 4.9 m, width e = 0.3 m, and thickness 1.8 cm with sand grains glued on its upper surface is set-up in the rectangular test section to characterize the clean wind flow avoiding interference from transported sand particles with the measuring equipment (see Fig. 1(b)). A ramp with gentle slope approximately equal to 3.1° is installed to smooth the transition between wind tunnel floor and the wooden board. In particular, the downwind edge of the wooden slab is located at the distance $a = 8h_{wt}$ from the inlet of the test section. Some initial exploratory tests with sand bed have been performed to ascertain the threshold velocity U_t, defined as the minimum value of the wind speed at which quasi-steady sand transport occurs at position d_3 (see Fig. 1b). In particular, wind speed is gradually incremented until quasi-steady transport is detected, i.e., the wind shear velocity is equal to the threshold one ($u_* = u_{*t}$), and the wind speed is acquired through a Pitot tube. During the wind tunnel test, the reference wind speed is set equal to U=

7.35 m/s ≈ 1.5U_t. With this setup (*Setup 0*, in the following), the wind speed profile $u(z,t)$ is measured over the wooden slab at positions d_2 = 3 m and d_3 = 4.5 m.

2.2 Wind-sand setup

Two wind-sand setup have been tested. *Setup A* implements a uniform flat sand bed (Figs. 2(a), 2(c)) while *Setup B* results from Setup A by installing the sinusoidal hill model downwind the flat sand bed (Figs. 2(b), 2(d)).

A flat sand bed of length c = 4.9 m, width b = 1.8 m, and thickness 1.8 cm is set-up in the wind tunnel test section replacing the wooden slab in Setup 0 (see Fig. 2(a)). The sand bed is confined by wooden slats and filleted to the wind tunnel floor through the upwind ramp in analogy with the setup proposed by Tominaga *et al*. (2018). Every test run started from the same initial condition, i.e., a perfectly flat uniform sand bed, and lasted Δt = 300 s to ensure the reaching of a quasi-steady sand transport. During the test on Setup A, the sand particles velocity $u_s(z,t)$ and concentration $\varphi(z,t)$ profiles are measured at positions d_1= 1.5 m, d_2 = 3 m, and d_3 = 4.5 m (see Figs. 2(a) and 2(c)).

In Setup B, the scale model of the hill is installed downwind the 4.9 meter long sand fetch. The model is made of wooden ribs over which a plexiglas sheet is applied in order to dampen the scatter resulting from the laser sheet adopted for optical measurements (see Fig. 2(b)). The hill elevation follows the sinusoidal profile $z_b = \frac{h}{2}\sin\left[\frac{2\pi}{l}\left(x - \frac{l}{4}\right)\right] + h/2$, being h =0.15 m the hill height and l = 1 m the hill length in the streamwise direction (see Fig. 2(d)). The width b of model corresponds to the width of the sand bed. The resulting model Aspect Ratio is then equal to AR = b/h = 12. Two end plates are placed next to the lateral free-ends of the model to reduce end-tip aerodynamic effects and confine the upwind sand fetch. The right-sided end plate is made of transparent plexiglas to allow optical measurements. Eight consecutive test runs of duration Δt = 300 s have been performed in order to simulate the progressive filling of the hill model: from the initial condition at t = 0 (i.e., uniform flat sand bed) to t = 2400s (i.e., maximum accumulation of sand around the hill). After each test run, the sand source is uniformly replenished when an eroded patch is identified over the upwind sand fetch to avoid unintended variations on the incoming sand flux due to the lack of sand source. It is worth stressing that sand bed was replenished only in the area between 1.5 and 5 m upwind the hill model so as not to alter the profile of sedimented sand in proximity of the hill model. During the test on Setup B, the sand particles velocity $u_s(z,t)$ and concentration $\varphi(z,t)$ that overcome the top of the sinusoidal hill, as well as the evolution of the sand bed profile upwind the sinusoidal hill are measured (see Fig. 2(d)).

The particle size distribution of the tested sand is obtained through microscopic imaging technique and is plotted in Fig. 3 through its cumulative distribution $F(d)$. The mean grain diameter is equal to $\bar{d}$= 0.147 mm. The threshold shear velocity of the tested sand resulted equal to u_{*t} = 0.245 m/s. Such a value agrees well with past wind tunnel measurements on sand samples of the same $\bar{d}$

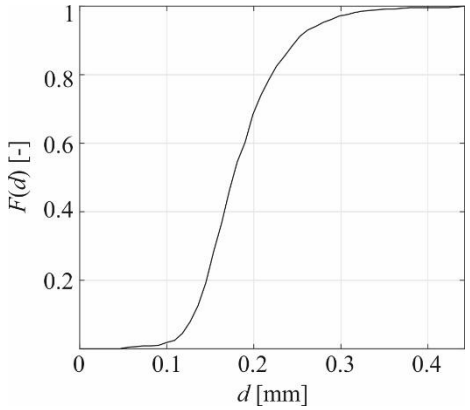

Fig. 3 Cumulative distribution of sand granulometry.

(Raffaele *et al*. 2016).

The wind-sand setup is designed by referring to typical in-field low roughness sandy desert/coast conditions. The following prototype features of wind flow and tested geometry are considered: (i) an open-field aerodynamic roughness z_0 = 4e-3 m; (ii) a mean threshold shear velocity u_{*t} = 0.245 m/s corresponding to the tested mean grain diameter $\bar{d}$= 0.147 mm; (iii) a wind shear velocity higher than the threshold and equal to $u_* = 1.5u_{*t}$; (iv) a characteristic height of the sinusoidal hill equal to h = 1.5 m. Concerning Setup A, the similarity of the saltation layer with respect to open field condition shall be ensured. In particular, this is pursued by:

• assuring that the wind flow during saltation is fully rough, i.e., the friction Reynolds number satisfies the criterion $\mathrm{Re}_* = u_*^3/2g\nu > 30$ (Anno 1984), being g and ν the acceleration of gravity and the air kinematic viscosity, respectively;

• avoiding disturbance in streamwise pressure gradient by satisfying the Froude number criterion, i.e., $\mathrm{Fr} = U^2/h_{wt}g < 20$ (White 1996);

• ensuring the similarity in motion of transported sand particles by matching the particle Shields number $\rho u_{*t}^2/(\rho_s - \rho)g\bar{d}$ (e.g., Zhou *et al*. 2014) where ρ and ρ_s are the air and sand particles densities respectively, expressing the ratio of cohesive force to gravity, and the ratio u_*/u_{*t} of aerodynamic to cohesive force (e.g., Anno 1984);

• adopting a sufficiently long sand fetch to ease sand transport saturation and let the wind flow adjust to the sand aerodynamic roughness z_0 over the fetch length (Kok *et al*. 2012).

Concerning Setup B, the similarity of windblown sand transport and accumulation around the sinusoidal hill with respect to full scale prototype conditions shall be provided. This is taken into account by referring to the ratio of the saltation layer thickness to the model height δ_s/h, and the well-known setup dimensionless numbers $\bar{d}/h$, Re, and Fr, governing the similarity of geometry, wind flow and particle trajectory. Furthermore, the wind tunnel setup shall always be designed by complying with acceptable values of the Blockage Ratio (BR) and Aspect Ratio (AR).

Similarity requirements intended to reproduce windblown sand transport and sedimentation around

Table 1 Setup dimensionless parameters of wind-sand tunnel Setup A and Setup B

Wind-sand tunnel setup	Similarity requirement	Expression	ϕ_m	ϕ^*
Setup A - flat sand fetch	Friction Reynolds number	$u_*^3/2g\nu > 30$	172	1
	Wind tunnel Froude number	$U^2/h_{wt}g < 20$	2.8	-
	Shields number	$\rho u_{*t}^2/(\rho_s - \rho)g\bar{d}$	4.5e-2	1
	Effective shear velocity	u_*/u_{*t}	1.5	1
Setup B – sinusoidal hill	Blockage ratio	$bh/w_{wt}h_{wt} < 0.05$	4.5e-2	-
	Aspect ratio	b/h	12	-
	Geometric similarity	$\bar{d}/h$	9.8e-4	10
	Reynolds number	hU/ν	7.4e+4	0.14
	Froude number	U^2/hg	36.7	20
	Saltation to model height ratio	δ_s/h	~0.3	~2.5

ground-mounted obstacles are seldomly all satisfied. Indeed, a perfect matching of similarity requirements remains impracticable in conventional wind tunnel facilities due to the multiphase flow and the multiscale features of the problem ranging from the sand grain to the obstacle characteristic lengths and to the wind field scales, as pointed out in Sherman (2020). However, setup dimensionless numbers are herein provided in order to shed some light on such limitations and draw some general remarks in a wind tunnel setup design perspective. The considered similarity parameters for both Setup A and Setup B are summarized in Table 1 through the generic model dimensionless number ϕ_m and the ratio between model and prototype dimensionless numbers $\phi_* = \phi_m/\phi_p$. On the one hand, ϕ_* should be as close as possible to 1. On the other hand, low values of BR are recommended in general while high values of AR are preferable for nominally two-dimensional geometries in order to limit and circumscribe end-tips aerodynamic effects. In the following, the main remarks are listed.

• Windblown sand transport similarity in open-field conditions (Setup A) can be addressed in wind-sand tunnel tests. The most strict requirement is related to the height of the wind tunnel test section, affecting the wind tunnel Froude number. However, large wind tunnel facilities easily meet this criterion.

• The geometric scaling of the hill model results in satisfactory values of BR and AR. However, geometric similarity is impracticable to be matched given the impossibility of scaling the sand grain diameter $\bar{d}$ without altering interparticle forces and the threshold velocity, in turn (see e.g., Raffaele *et al*. 2016).

• Re number is underestimated while Fr number is overestimated due to the impossibility of tuning freely the reference wind speed *U*. However, the value of Re number suggests that the flow is just in correspondence of the initiation of the supercritical regime for two-dimensional sinusoidal hills (see Ferreira *et al*. 1995).

• The saltation layer thickness δ_s is mostly related to the sand grain diameter *d* and it is typically higher in the field than in wind-sand tunnel tests (Martin and Kok 2017). In particular, under prototype conditions $\delta_s \approx 20$ cm while in wind-sand tunnel tests $\delta_s \approx 5$ cm (Raffaele *et al*. 2022). The impossibility of scaling freely the saltation layer height in wind tunnels leads to a discrepancy of the ratio δ_s/h between model and prototype of the order of about 2.5.

Overall, setup dimensionless parameters provided in Table 1 confirm that a perfect matching remains impracticable in conventional wind tunnel facilities. As a result, distortion between model and full-scale windblown sand state variables can be expected. According to the authors, the entity of such a distortion is mainly related to the ratio δ_s/h (Raffaele *et al*. 2021). In this study, model dimensions are set in order to meet similarity requirements, wherever possible.

2.3 Measuring systems

The adopted measuring systems are the same for every setups, i.e., Setup 0, Setup A and Setup B. The wind velocity field is measured via 2D Particle Image Velocimetry (PIV) technique adopting a smoke generator to seed the flow with oil particles ranging from 1e-3 mm to 5e-3 mm. The sand particles velocity is measured via 2D Particle Tracking Velocimetry (PTV) technique being the most reliable one for saltation (Creyssels *et al*. 2009). Sand particles are identified from PTV pictures through a particle detection algorithm based on intensity gradient. In particular, sand concentration is obtained by dividing the transported sand particles volume by the air control volume V_c through the following relation $\varphi = \pi\bar{d}^3 N/6V_c$, being *N* the number of particles for each V_c, in analogy to Zhang *et al*. (2010). Finally, the morphodynamic evolution of the wind-sand interface is assessed by detecting the profile of laser scattered by the sandy surface. Each measurement is taken along the test section centreline so that the influence of boundary layer developed on the lateral sides of the wind tunnel and end plates is minimized.

The measuring section positioning differs both depending on the setup and depending on the adopted technique, i.e., PIV or PTV. In Setup 0 and Setup A, a 200 mJ Nd:YAG laser source is located far downwind the sand fetch. This allowed to generate a wide laser sheet along the test section centreline and perpendicular to the floor reaching the measuring section in d_1. During PTV

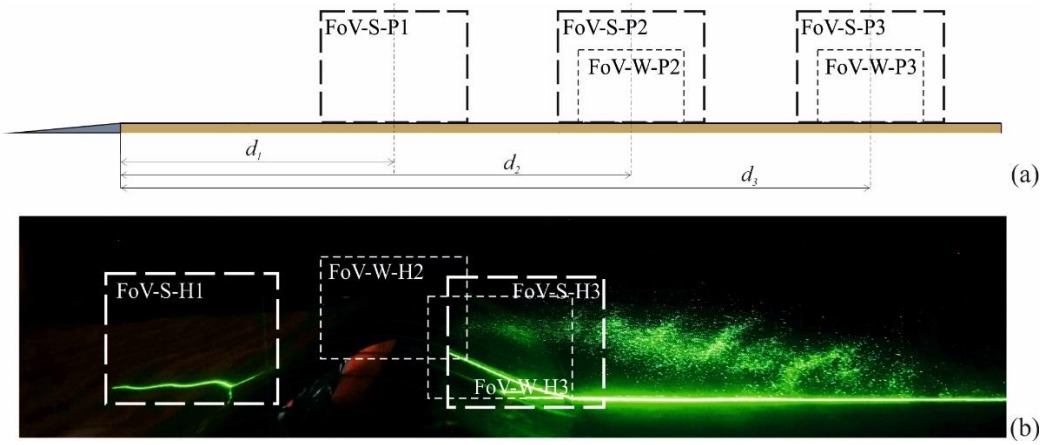

Fig. 4 Location of Field of Views (FoVs) for wind and sand fields measurements: flat plane (a) and hill model (b)

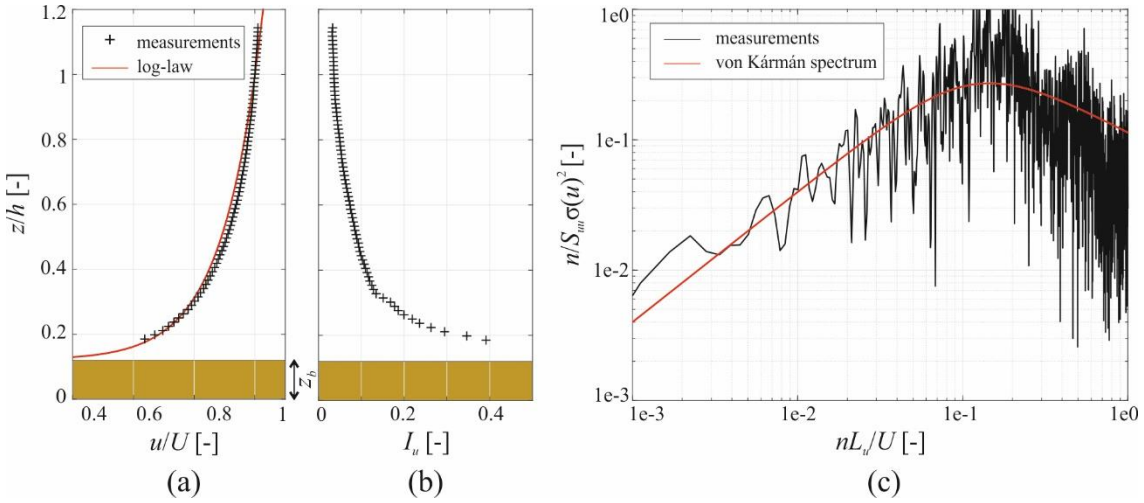

Fig. 5 Normalized incoming longitudinal mean velocity profile u (a), turbulence intensity profile I_u (b) and normalized power spectral density of longitudinal turbulence fluctuations S_{uu} (c)

measurements, the thickness of the laser sheet resulted equal to 8.6 mm, 7.2 mm, 5.4 mm at positions d_1 = 1.5 m, d_2 = 3 m, and d_3 = 4.5 m from the upwind edge of the wooden slab, respectively. In Setup B, the same laser source is located on the ceiling of the testing chamber. During PTV measurements, a 7.5 mm thick laser sheet is generated along the test section centreline and perpendicular to the floor. In every setup, the laser source was pulsating at 10 Hz for PIV and 2 Hz for PTV.

Two CMOS cameras with resolution 2360 × 1776 pixels are located outside the test section. Their Field of View (FoV) are sketched in Fig. 4. In particular, FoV-W stands for FoV devoted to capture wind field, while FoV-S stands for FoV devoted to measured sand-related variables. Over flat plane conditions, the wind velocity field is captured through a 50 mm objective ensuring an 18×14 cm^2 FoV (FoV-W-P2 and FoV-W-P3, Fig. 4(a)) while the velocity and concentration fields of incoming sand particles are captured through a 35 mm objective ensuring a 55 × 40 cm^2 FoV (FoV-S-P1, FoV-S-P2 and FoV-S-P3, Fig. 4(a)). Over the hill model, the wind velocity field is captured through a 40 mm objective ensuring a 40 × 30 cm^2 FoV (FoV-W-H2 and FoV-W-H3, Fig. 4(b)) while the morphodynamic evolution of the upwind sand bed (FoV-S-H1, Fig. 4(b)) as well as the velocity and concentration fields of passing sand particles are captured through a 35 mm objective ensuring a 55 × 40 cm^2 FoV (FoV-S-H3, Fig. 4(b)).

3. Results

In the following, the clean wind flow features are presented, then sand transport and sand bed morphodynamics are discussed by differentiating between incoming flow features and flow features around the sinusoidal hill. Finally, the sedimentation performance of the hill model is evaluated through a synthetic dimensionless metric.

3.1 Wind flow characteristics: undisturbed flow and flow over the hill

The undisturbed wind flow, i.e., not affected by the hill model, is characterized in Setup 0 at location d_3, i.e., at 15.5 m from the inlet of the test section. In particular, the profiles of the mean wind speed $u(z)$ and turbulence

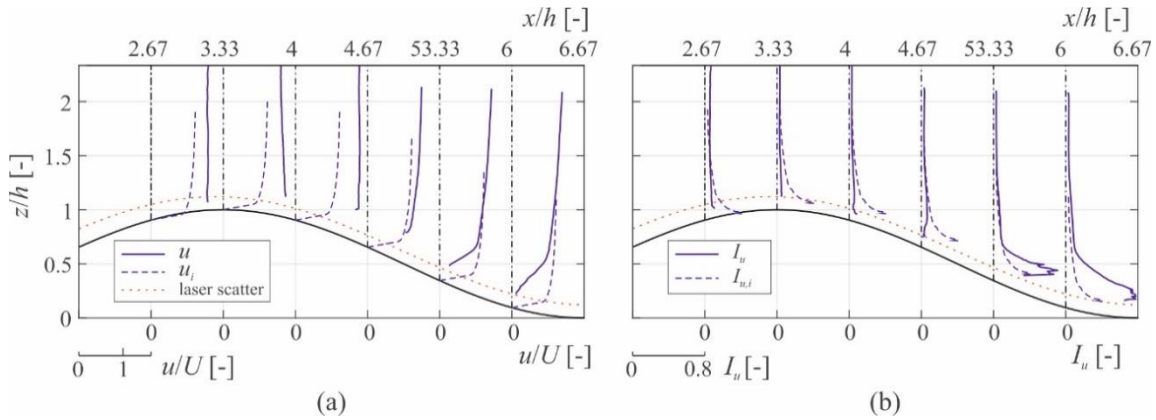

Fig. 6 Normalized longitudinal mean velocity (a) and turbulence intensity (b) profiles over the sinusoidal hill, with respect to undisturbed flow

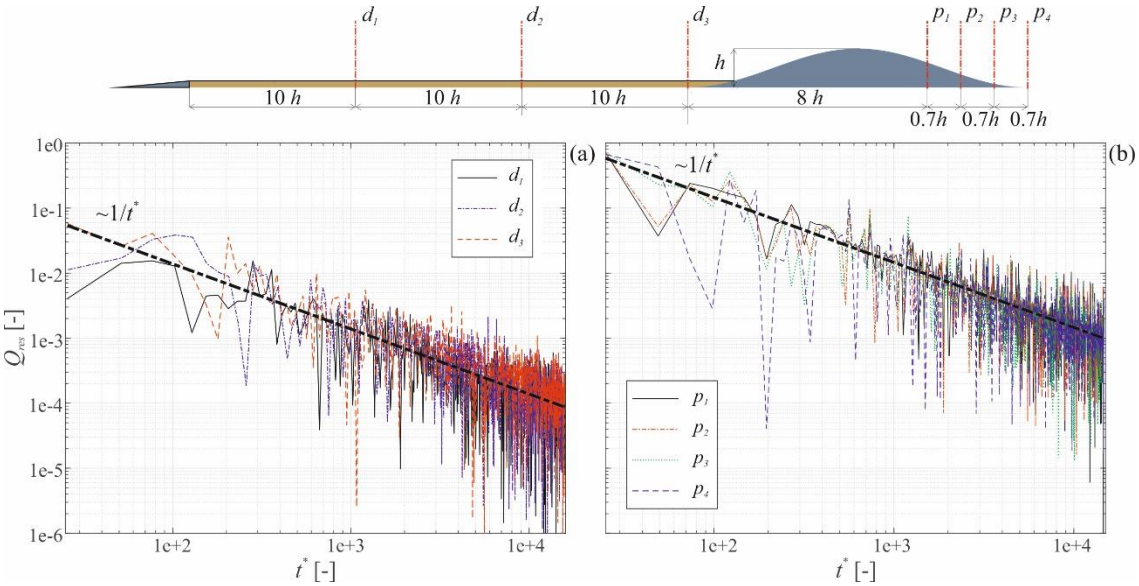

Fig. 7 Convergence of the sand transport rate Q through the weighted residuals Q_{res} for Setup A and Setup B ($t^* \in [0,1.5e+4]$)

intensity $I_u(z)$ are obtained and then compared with the profiles measured over the hill. The same measurements were carried out at location d_2 showing good agreement. As a result, boundary layer is considered fully developed and the effect of the streamwise pressure gradient is deemed too small to affect boundary layer separation over the hill. The undisturbed wind flow characteristics at location d_3 are shown in Fig. 5. The mean wind speed profile normalized by the mean speed at the reference height h, U = 7.35 m/s, is plotted in Fig. 5(a). The boundary layer thickness δ is approximately equal to the height of the hill model h. The aerodynamic roughness z_0 as well as the wind shear velocity u_* are determined by fitting the log-law $u(z) = u_*/\kappa \cdot \ln((z - z_b)/z_0)$, being κ = 0.41 the von Kármán constant and z_b the height of the wooden slab, resulting z_0=9e-5 m and u_* = 0.4 m/s.

The flow roughness Reynolds number is equal to $\mathrm{Re}_* = u_* z_0/\nu = 1.7$, i.e., lower than the lower limit for fully rough flows Re_* = 2.3 proposed by Snyder and Castr (2002). As a result, the clean undisturbed wind flow falls into the transitional regime, i.e., viscous effects are not completely negligible in the region above the roughness. The streamwise turbulence intensity profile is shown in Fig. 5(b). In particular, turbulence intensity at the hilltop is very low and equal to 3.5%. In Fig. 5(c), the power spectral density S_{uu} of the longitudinal component of velocity fluctuations measured at the height z = 0.37 m and estimated under Taylor's frozen-eddy hypothesis is shown in normalized units versus the dimensionless frequency. In particular, n = 1.6e+4 Hz is the Pitot sampling frequency and L_u= 0.18 m is the characteristic length scale of the longitudinal turbulence component. Measurements show the typical -2/3 slope in the inertial subrange predicted under Kolmogorov's hypothesis and are in overall good agreement with the power spectral density expression proposed by von Kármán (von Kármán 1948), even if measurements show a slightly larger dissipation at high frequencies.

The wind flow characteristics over the hill are shown in Fig. 6. The undisturbed flow profiles (u_i, $I_{u,i}$) are included

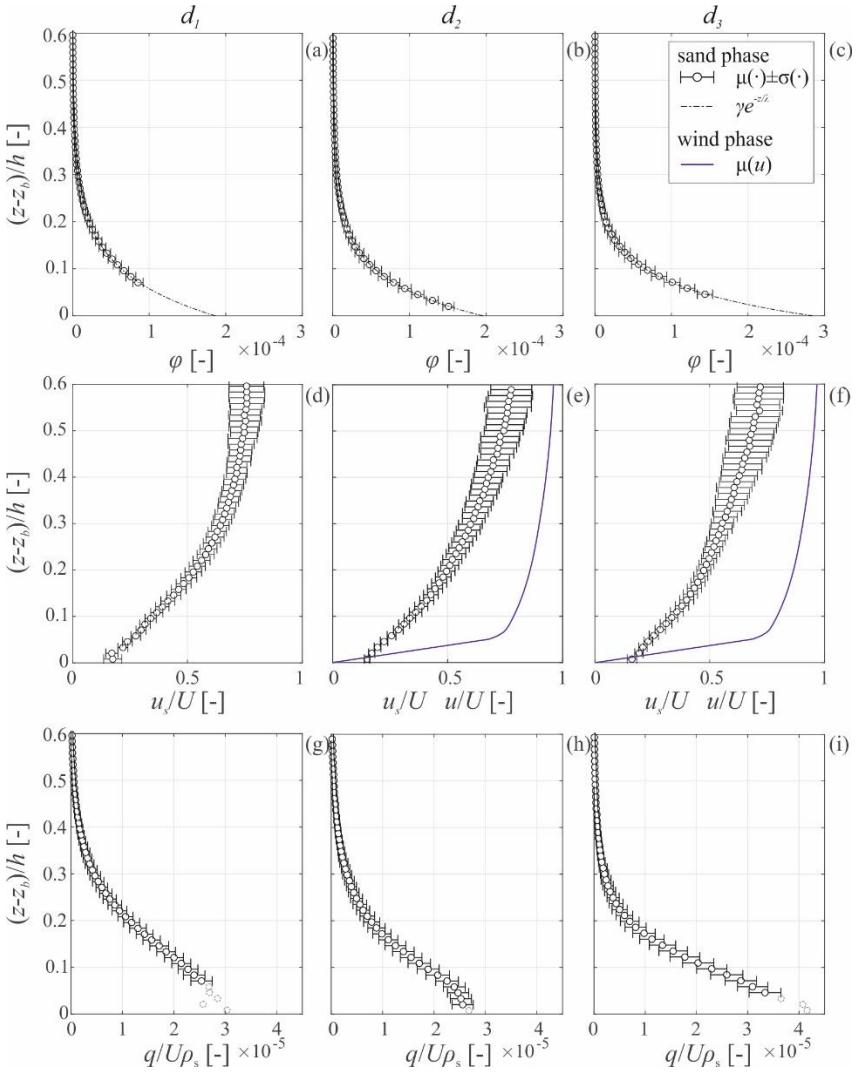

Fig. 8 Vertical profiles of sand concentration φ (a-c), longitudinal velocity u_s (d-f), and resulting flux q (g-i) at locations d_1 (a, d, g), d_2 (b, e, h), and d_3 (c, f, i)

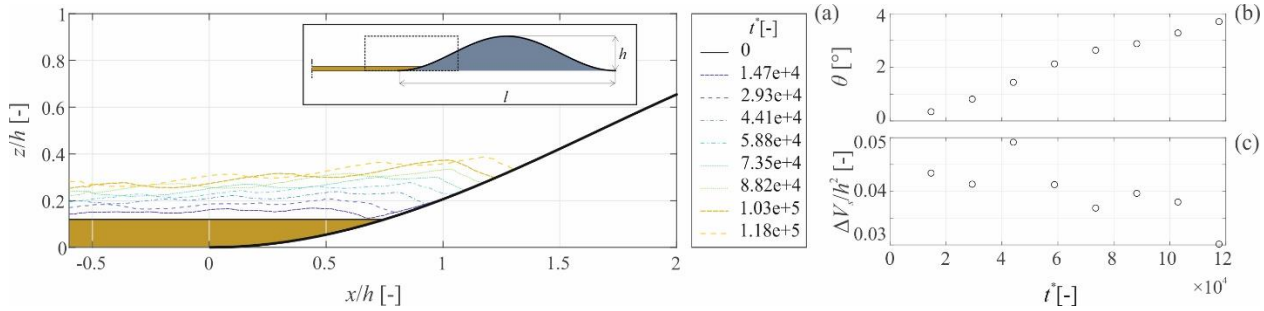

Fig. 9 Morphodynamic evolution of the sand bed over the hill upwind slope (a), time-varying sand bed slope θ (b), and volume V_s (c)

for reference purposes. Despite the adopted precautions during wind tunnel testing, laser reflection prevented the correct assessment of the flow field approximately up to 2 cm from the hill surface. As a result, wind tunnel measurements below 2 cm are missing. Fig. 6(a) compares the vertical profiles of mean velocity at six downstream locations over the hill model with the vertical profile of the incoming mean wind speed. The wind speed is normalized with respect to the reference wind speed U. The flow significantly accelerates at the hilltop, with respect to the incoming wind speed profile. On the downwind side of the hill, wind speed profiles largely deviate from the reference profile because of the reversed flow region induced by the hill slope. In particular, the maximum hill slope is equal to 25°, that is higher than the critical value 16° for boundary layer separation suggested by Finnigan (1988). Fig. 6(b)

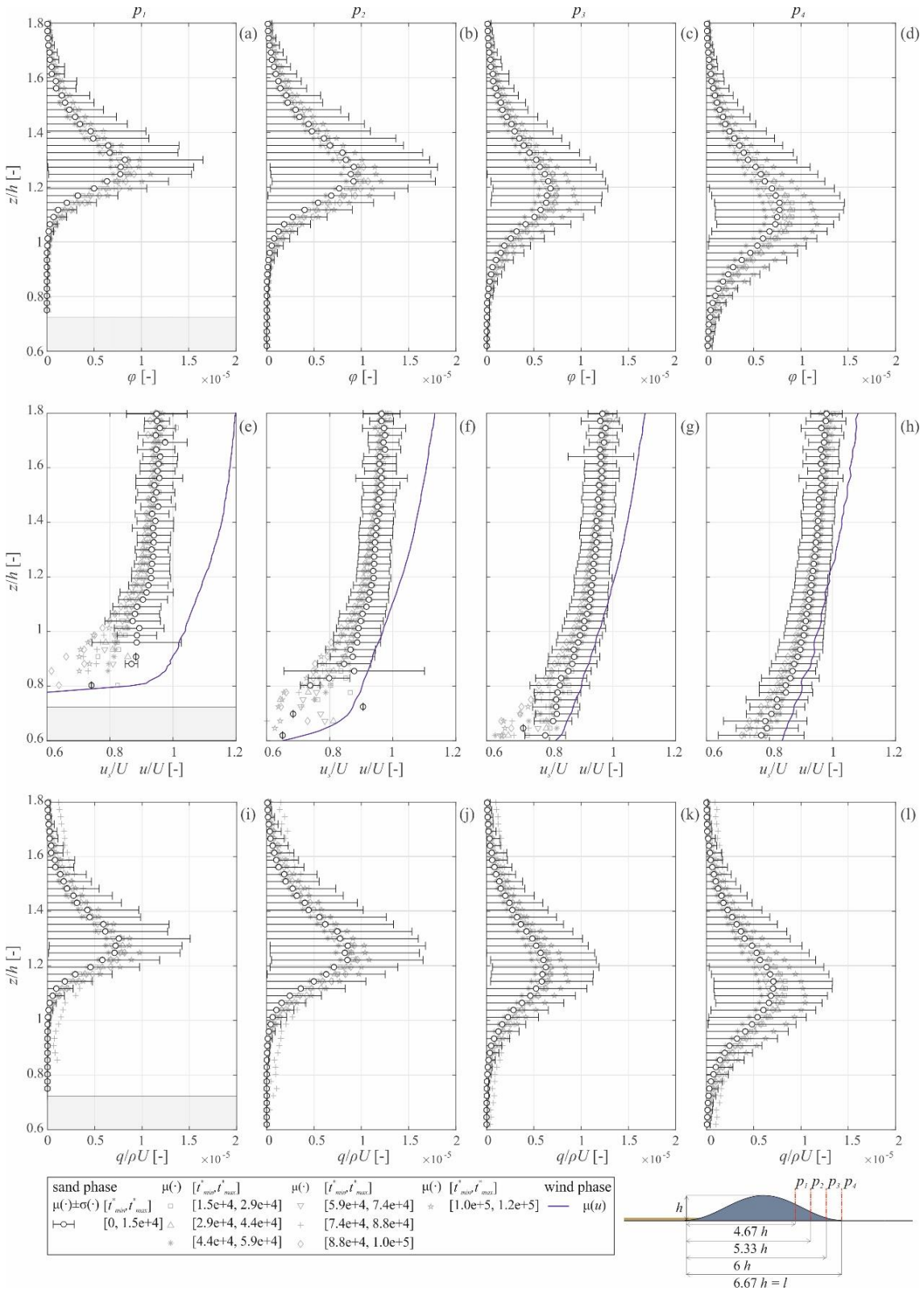

Fig. 10 Vertical profiles of sand volume fraction φ (a-d), velocity u_s (e-h), and flux q (i-l) at positions p_1 (a,e,i), p_2 (b,f,j), p_3 (c,g,k), and p_4 (d,h,l)

shows the profiles of the streamwise turbulence intensity at the same locations together with the vertical profile of the undisturbed turbulence intensity. On the hilltop, velocity fluctuations close to the wall are lower with respect to undisturbed values. According to the authors, this is induced by the smooth surface of the hill surface compared to the rough sandy layer spread over the wooden slab. Conversely, velocity fluctuations on the downwind side increase due to

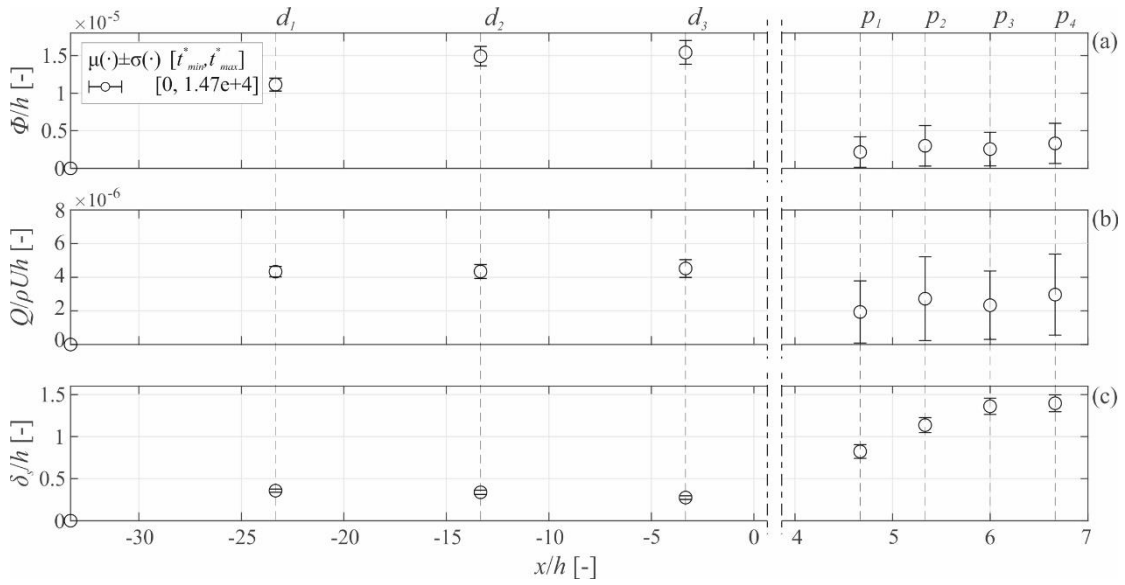

Fig. 11 Streamwise variation of average sand bulk concentration Φ (a), transport rate Q (b) and saltation layer thickness δ_s (c)

the shear layer induced by boundary layer separation (e.g., Cao and Tamura 2006) highlighting that separation occurs very close to the wall.

3.2 Sand transport characteristics and morphodynamics

Preliminarily, the time convergence of sand transport rate is ascertained. The average incoming sand transport rate over the flat sand bed and passing sand transport rate over the hill model result equal to $\bar{Q} = \frac{1}{t}\int_0^t \int_0^{+\infty} \rho_s \bar{\varphi}(z,\tau)\bar{u}_s(z,\tau)\, dz\, d\tau$, being t the testing time, ρ_s = 2650 kg/m^3 the sand grains density, $\bar{\varphi}$ the average sand concentration in air, and $\bar{u}_s$ the average sand grains longitudinal speed. Convergence is checked by means of the weighted residual Q_{res} of $\bar{Q}$ for increasing dimensionless time t^* = tU/h at all locations at which measurements are carried out.

The weighted residual is defined for growing t^* as $Q_{res}(t^*) = |\bar{Q}(t^*) - \bar{Q}(t^* - \Delta t^*)|/\bar{Q}(t^*)$, being Δt^* the time interval between consecutive PTV acquisitions. Obtained results are plotted in Fig. 7 for Setup A (a) and Setup B (b) over $t^* \in [0,1.5e+4]$. When $t^* = 1.5e+4$, $Q_{res} \approx 1e-4$ for each location in Setup A while $Q_{res} \approx 1e-3$ for each location in Setup B. Such residuals are low enough for engineering applications. However, this highlights the longer time required to reach convergence in sand transport rate over the hill where the flux is not in equilibrium with respect to sand transport on flat plane conditions. It is worth stressing that, despite the discrepancy in residuals magnitude between Setup A and Setup B, the convergence rate is the same and it is equal to $\sim 1/t^*$, in agreement with Raffaele *et al.* (2021, 2022).

Fig. 8 collects the vertical profiles of the sand concentration in air $\varphi(z)$, the longitudinal component of the sand grains velocity $u_s(z)$, and the resulting flux $q(z)$ in dimensionless units at locations d_1 (a,d,g), d_2 (b,e,h), and d_3 (c,f,i) of Setup A, through their mean value μ and standard deviation σ.

It is worth highlighting that, due to non-uniformity in the laser reflections along the *x*-axis, the trend of $\varphi(z)$ was not fully resolved close to the wall. Both $\mu(\varphi)$ and $\sigma(\varphi)$ increase with decreasing *z*. Sand concentration follows the well-known exponentially decreasing trend $\mu(\varphi(z)) = \gamma e^{-z/\lambda}$, being γ and λ fitting constants (Ho *et al.* 2011). Furthermore, $\mu(\varphi)$ varies along the *x*-axis by incrementing the value at the wall.

The longitudinal component of sand grain velocity is directly assessed through PTV algorithm. Fig. 8(e,f) includes the longitudinal component of the average wind speed obtained at the same locations in Setup 0, for reference purpose. The vertical profile of $\mu(u_s)$ can be divided into two layers (Valance *et al.* 2015). Within the near-wall layer ($z/h < 0.2$), $u_s(z)$ linearly increases with *z*. Due to the high $\varphi(z)$, $u_s(z)$ is mainly driven by the bounce of the sand grains at the sand surface. Indeed, u_s is not nil at the wall. Conversely, for $z/h > 0.2$, $u_s(z)$ follows a logarithmic-like increasing trend. The low values of $\varphi(z)$ do not significantly affect the wind flow and u_s, in turn. Accordingly, $\sigma(u_s)$ progressively increases with increasing *z*.

The longitudinal sand flux directly results from $q(z) = \rho_s \varphi(z) u_s(z)$. Close to the wall, missing values of $q(z)$ due to the non-fully resolved profile of $\varphi(z)$ are extrapolated from the fitted exponentially decreasing functions of sand concentration (see grey dotted circles in Figs. 8(g)-8(i). Similarly to φ, both $\mu(q)$ and $\sigma(q)$ increase with decreasing *z*. The measured profiles evolve towards a typical monotonic decreasing exponential trend (Kok *et al.* 2012) and exhibit a growth of the value at the wall from d_1 to d_3.

During the test on Setup B, the sand eroded along the flat sand fetch progressively sediments upwind the hill model and over the hill upwind slope despite the presence

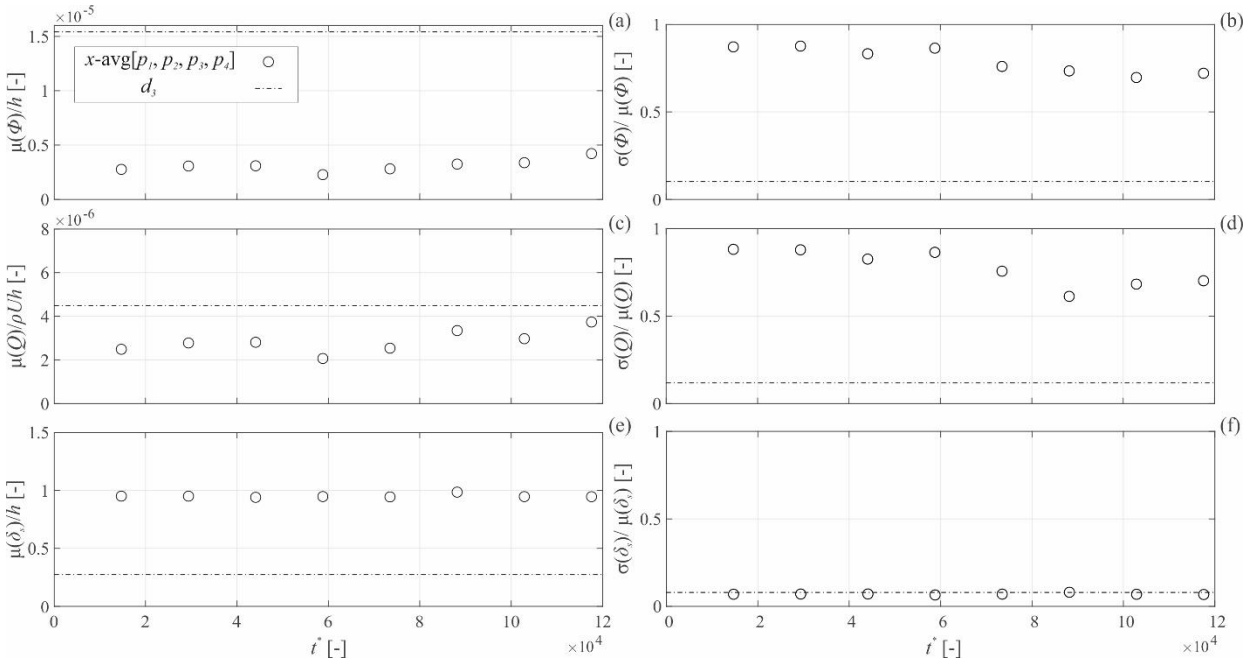

Fig. 12 Variation over time of sand bulk concentration Φ (a,b), transport rate Q (c,d) and saltation layer thickness δ_s (e,f) through their mean values and coefficients of variation

of a low-speed recirculation zone over the hill downwind side. This is the result of the lunch-pad effect induced by the hill upwind slope which allows the sand grains to completely overcome the low-speed zone in the wake of the hill model (see Fig. 10). It is worth stressing that wind flow features depicted in Fig. 6 are obtained without simultaneous sand transport. As a result, they definitely vary during saltation due to the absorption of wind momentum by sand particles. The near-wall absorption of wind momentum is perceived by the wind boundary layer flow as an increment of the aerodynamic roughness (Sherman and Farrell 2008). Since the aerodynamic roughness determines the properties of upstream turbulence, we can conjecture that the increment of upstream roughness reduces the size of the recirculation region because of the reduction in wind momentum and the increment in turbulence intensity (Essel *et al*. 2015).

The morphodynamic evolution of the sand bed upwind the hill model is plotted in Fig. 9(a). The sand bed progressively increases in height over the whole investigated length and climbs over the hill upwind slope. Sand sedimentation is induced by the typical wind speed deceleration taking place over the upwind side of hill-shaped obstacles. Windblown sand transport induces the formation of wind ripples along the wind-sand interface, as testified by the wavy profiles. It is worth stressing that ripples formation (including modifications of ripple length, height, and migration rates) is one of the key elements showcasing the reaching of equilibrium state in windblown sand transport (Sherman *et al*. 2019). Figs. 9(b), 9(c) shows the time-varying average slope θ of the wind-sand interface and the variation of the accumulated sand volume $\Delta V_s = V_s(t^*) - V_s(t^* - \Delta t^*)$ per span unit, being $\Delta t^* = 1.47e{+}4$, assessed within the FoV showed in Fig 9(a). In particular, θ progressively increases while ΔV_s progressively decreases for increasing t^*. The decreasing trend of ΔV_s denotes the progressive reaching in-equilibrium sand transport conditions over the hill profile. According to the authors, the discontinuous changes in ΔV_s are caused by the inborn variability of windblown sand processes (Sherman 2020), and to the fact that ΔV_s is evaluated just within FoV-S-H1 (see Fig. 4). Conversely, the persistent increase of θ highlights that the wind-sand interface did not fully reach equilibrium conditions during the wind-sand tunnel test duration.

Fig. 10 collects the vertical profiles of the sand concentration in air $\varphi(z)$, the longitudinal component of the sand grains velocity $u_s(z)$, and the resulting flux $q(z)$ over the sinusoidal hill at positions p_1 (a,e,i), p_2 (b,f,j), p_3 (c,g,k), and p_4 (d,h,l) in dimensionless units and averaged over the duration of each test run, $\Delta t^* = 1.47e + 4$, on Setup B. In particular, measurements obtained during the first test run are plotted through their mean value and standard deviation in black while the others are plotted in grey colour through their mean value only.

The general trends of $\varphi(z)$, $u_s(z)$ and $q(z)$ are not affected sensibly by t^*. The trend of mean value and standard deviation of φ and q are non-monotonic, exhibiting a peak within $z/h \in [1,1.3]$. The sand flux profiles mainly follow the trend of sand concentration ones given the slight variation of u_s along z. In particular, the peak in mean value and standard deviation of φ and q progressively decreases when moving along the x-axis, i.e., sand particles progressively fall due to gravity following a ballistic trajectory. Furthermore, the profiles φ and q progressively modify along the x-axis switching from narrow spread to widespread distributions. According to the authors, this reflects the progressive spreading of sand particles induced by the inborn randomness of sedimentation velocity (Raffaele *et al*. 2020) and turbulent

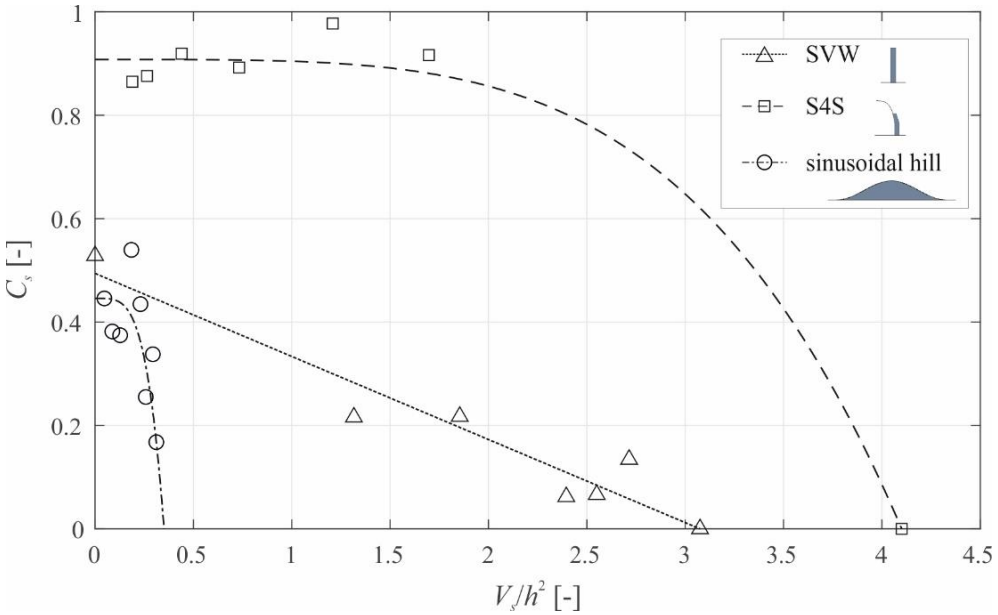

Fig. 13 Comparison between sedimentation coefficients of tested sinusoidal hill, Straight Vertical Wall (SVW, from Hotta and Horikawa 1991), and Shield for Sand (S4S, from Raffaele *et al.* 2021)

diffusion. Conversely, the general trend of $\mu(u_s)$ is slightly increasing with increasing z, while $\sigma(u_s)$ is slightly decreasing. Figs. 10(e), 10(f), 10(g), 10(h) includes the longitudinal component of the mean wind speed obtained at the same locations without simultaneous sand transport, for reference purpose. For low values of z, $\mu(u_s)$ linearly increases with z and roughly follows the trend of $u(z)$. Here, $\sigma(u_s)$ is larger mainly because of the low cardinality of particles transported at this height. For larger values of z, $u_s(z)$ deviates from $u(z)$ reaching a vertical upper asymptote. According to the authors, the slight variation of u_s along z is justified by the values of $\varphi(z)$, that is low enough not to affect the wind velocity field and the sand particle speed, in turn. Indeed, peaks in $\mu(\varphi)$ over the hill model are more than one order of magnitude lower than the maximum concentration values attained on flat plane conditions (see Fig. 8 for comparison). It is worth noticing that sand particles very slightly speed up from p_1 to p_4 while the wind speed progressively decreases. This reflects that sand transport is affected by particles inertia. For a given height, the magnitude of φ and q varies with t^* while the magnitude of u_s is roughly constant, especially far from the wall. Conversely, small variations in u_s can be observed where $z/h < 1$. In general, $u_s(z)$ slightly decreases for increasing t^*. According to the authors, sand particle speed variations are induced by the progressive sedimentation of sand over the hill upwind slope, affecting particles trajectory, in turn. It is worth pointing out that variability in windblown sand transport over the hill is higher than variability measured over the flat sand bed. This is the result of the perturbation to in-equilibrium windblown sand transport induced by the obstacle and the concurrent sedimentation occurring over the hill upwind slope.

In the following, the streamwise and temporal variation of sand transport is analyzed by referring to bulk metrics summarizing key features of the vertical profiles showed in Fig. 8 and 10. In particular, we defined the bulk concentration $\Phi = \int_0^{+\infty} \varphi(z)\, dz$, transport rate $Q = \int_0^{+\infty} q(z)\ dz$, and thickness of saltation layer $\delta_s = z_s - z_b$, being z_s the saltation layer height at which $\int_{z_b}^{z_s} q\ dz / \int_{z_b}^{+\infty} q\ dz = 0.95$ and z_b the ground height. Fig. 11 collects the streamwise variation of the bulk metrics averaged within the first test run, i.e., $t^* \in [0,1.47e+4]$, in dimensionless units.

The bulk concentration gradually increases over the flat sand fetch indicating the progressive reaching of in-equilibrium conditions in position d_3 where $\mu(\Phi)/h \approx 1.5e{-}5$. Over the hill model, sand concentration suddenly decreases to roughly constant values around $\mu(\Phi)/h \approx 0.3e{-}5$. Similarly, the trend of sand transport rate over the flat sand fetch denotes the reaching of in-equilibrium conditions corresponding to $\mu(Q)/\rho U h \approx 4.5e{-}6$. Sand flux is then halved over the hill model due to sand sedimentation over the hill upwind foot. However, fluctuations in Q are larger than the ones in Φ because of the contribution of u_s. The saltation layer thickness increases and then gradually decreases over the sand bed, resulting equal to about $\mu(\delta_s) \approx 0.3h$ under in-equilibrium conditions at position d_3. Then, it suddenly increases over the hill profile approaching $\mu(\delta_s) \approx 1.5h$ due to the launching pad effect induced by the hill model. Overall, plots in Fig. 11 confirm the reaching of in equilibrium conditions over the flat sand fetch, and a sudden modification in sand transport features triggered by the hill profile. In particular, while the bulk concentration and sand transport rate are constants over the hill profile, the saltation layer height varies along the x-axis due to the opposed effects of falling trajectory of sand particles and lowering of z_b.

Fig. 12 collects the variation over time of the same bulk variables averaged among positions p_1, p_2, p_3, and p_4,

distinguishing between mean values (a,c,e) and coefficients of variation (b,d,f). Measurements in position d_3 are included for reference purposes.

The trend of the computed statistics of Φ and Q is qualitatively similar: mean values globally increase while coefficients of variation globally decrease for increasing t^*, even if nonmonotonically. Their trends denote the progressive reaching of sand transport features under in-equilibrium conditions for high t^*. Quantitatively, $\mu(\Phi)$ values over the hill model remain by far lower than in position d_3 due to the lack of erodible sand source while $\mu(Q)$ over the hill model is closer to undisturbed conditions due to the speed-up of wind speed and sand particles, in turn. Conversely, coefficients of variation of Φ and Q are similar in magnitude. Finally, saltation layer thickness statistics are roughly constant over time despite the variation observed for Φ and Q. This means that the progressive sand accumulation taking place over the hill upwind slope does not sensibly affect saltation hop heights.

3.3 Sedimentation coefficient

The capability of the sinusoidal hill model to induce sedimentation is herein expressed by referring to incoming undisturbed transport rate on flat sand bed conditions and passing transport rate over the hill model. In particular, sedimentation capability is evaluated in average terms through the dimensionless sedimentation coefficient defined as:

$$C_s(t^*) = \frac{Q_i(t^*) - Q_p(t^*)}{Q_i(t^*)} \quad (1)$$

being Q_i and Q_p the incoming and passing sand transport rates, respectively. It is worth highlighting that $C_s \in [0,1]$, and high and constant values of C_s result in higher sedimented sand volumes V_s around the tested obstacle. In the case of human-built or natural obstacles, high and constant C_s is generally preferred for sand mitigation measures or coastal dunes beneficial for coastal protection, while low C_s is preferred for obstacles on which sedimentation effect is detrimental, i.e., civil structures and infrastructures (see e.g., Raffaele and Bruno 2019, 2020).

Fig. 13 shows the trend of C_s obtained from the tested sinusoidal hill together with other C_s values from the literature. In particular, it includes values obtained from wind-sand tunnel tests carried out on a basic Straight Vertical Wall (SVW, from Hotta and Horikawa 1991) and on the Shield for Sand (S4S, from Raffaele *et al*. 2021) sand mitigation design solution. C_s is plotted versus the normalized sedimented volume V_s/h^2, being h the height of the generic tested model. The discrete mean values of C_s are fitted through least squares method by monotonic decreasing curves to extrapolate the global trend of C_s. In general, C_s shows a decreasing trend, i.e., the larger the sedimented sand volume, the lower the amount of sand trapped by the generic obstacle, the larger the amount of transported sand overcoming it. However, different obstacles result in different trends (linear or parabolic) and in different values of sedimentation capability (C_s) and normalized capacity (V_s/h^2). The trend of C_s is the steepest in the case of the sinusoidal hill: it suddenly decreases after a short plateau within $V_s/h^2 \in [0,0.15]$. It is worth noting that the plateau corresponds to the nearly constant value of ΔV_s for low t^* (see Fig. 9(c)). Indeed, Q_s and ΔV_s are bonded by the relation $\Delta Q_s \propto \Delta V_s \rho_s / t$. The authors conjecture that the plateau is due to the temporary persistence of a low-speed zone over the upwind foot of the hill and the subsequent change of the wind flow pattern due to the evolving morphodynamics. The sinusoidal hill has the lowest sedimentation capability and capacity among the analyzed obstacle geometries. Even when V_s is nil, about 55% of sand carried by wind overcomes the obstacle while SVW and S4S geometries imply about 50% and 10% of passing sand transport, respectively. Furthermore, the maximum normalized capacity of the sinusoidal hill results equal to about 0.35, while SVW and S4S exhibit much larger values respectively equal to about 3 and 4. In other words, for a given obstacle height the sinusoidal hill geometry implies the lowest amount of sedimented sand among the analyzed ones. According to the authors, the low capability of the sinusoidal hill to induce sedimentation is the result of its different aerodynamic features with respect to the other tested bluff bodies. In particular, SVW and S4S induce a large upwind recirculation region because of the separation they induce at the upper free edge, while the sinusoidal hill only induces upwind wind speed lowering.

4. Conclusions

In the present study, the wind flow, sand transport and morphodynamic evolution of the sand bed over a nominally two-dimensional sinusoidal hill are experimentally characterized through wind-sand tunnel testing. The reaching of equilibrium transport conditions over the sand fetch is ascertained by assessing the variation of sand concentration, flux and thickness of saltation layer. A sinusoidal hill model is tested by investigating the wind-sand flow around it, namely the evolution over time and space of the sand bed elevation profile and the vertical profiles of sand concentration, velocity and flux. The incoming and outgoing sand transport rates are condensed into the dimensionless sedimentation coefficient synthesizing the sedimentation capability of the tested model. The sedimentation coefficient is then compared with other values obtained from different wind-sand tunnel tests in the literature suggesting poor sedimentation capability for the tested obstacle.

The understanding of windblown sand transport over a nominally two-dimensional sinusoidal hill is beneficial in order to shed some light over the non-equilibrium wind-sand flow features taking place over complex geometries, such as sand dunes and sand mitigation design solutions. The same measurements are well-suited to validate computational simulations of sand transport and morphodynamic evolution around ground-mounted obstacles given the lack of similar studies in the literature. It is worth stressing that measured state variables are expected to be affected by both undisturbed wind flow characteristics, i.e., incoming average wind speed and

turbulence fluctuations, and sand characteristics, i.e., sand grains diameter, given the impossibility of matching all similarity criteria of the multiphase/multiscale windblown sand flow.

In the light of the comments above, the following research perspectives arise. First, we would like to promote further experimental studies investigating windblown sand transport features and sedimentation pattern for different setup dimensionless numbers characterizing the multiphase/multiscale windblown sand flow. Secondly, in the case of hill-shaped sand mitigation solutions or coastal dunes, it is worth investigating how to improve their sedimentation capability. Thirdly, we would like to encourage the implementation of computational simulations, properly validated on the present wind-sand tunnel measurements, to investigate the effect, if any, of similarity mismatching on the full-scale behavior of the same tested geometry. The hybrid physical-computational modelling can be beneficial for a wide range of studies related to windblown sand transport, ranging from performance assessment of full-scale sand mitigation measures (Raffaele *et al*. 2022) to the protection and restoration of coastal sand dunes (Martínez *et al*. 2013).

Acknowledgments

The study is part of the MSCA-IF-2019 research project Hybrid Performance Assessment of Sand Mitigation Measures (HyPer SMM, hypersmm.vki.ac.be). This project has received funding from the European Union's Horizon 2020 research and innovation programme under the Marie Sklodowska-Curie grant agreement No 885985. The study has been jointly developed in the framework of the research project PROtection Technologies from Eolian Events for Coastal Territories (PROTEECT, www.proteect.polito.it). This project has received founding from Italian Ministry for University and Research (PON-FSE REACT-EU) and Politecnico di Torino. The experimental campaign has been developed in the framework of the Windblown Sand Modelling and Mitigation (WSMM, www.polito.it/WSMM) joint research, development and consulting group established between Politecnico di Torino and Optiflow Company.

References

Andreotti, B., Claudin, P. and Pouliquen, O. (2010), "Measurements of the aeolian sand transport saturation length", *Geomorphology*, **123**(3-4), 343-348. https://doi.org/10.1016/j.geomorph.2010.08.002.

Anno, Y. (1984), "Requirements for modelling of a snowdrift", *Cold Reg. Sci. Tech.*, **8**(3), 241-252. https://doi.org/10.1016/0165-232X(84)90055-7.

Bitsuamlak, G., Stathopoulos, T. and Bédard, C. (2006), "Effects of upstream two-dimensional hills on design wind loads: A computational approach", *Wind Struct.*, **9**(1), 37-58. http://dx.doi.org/10.12989/was.2006.9.1.037

Bitsuamlak, G., Stathopoulos, T. and Bédard, C. (2004), "Numerical evaluation of wind flow over complex terrain: Review", *J. Aerospace Eng.*, **17**(4), 135-145. https://doi.org/10.1061/(ASCE)0893-1321(2004)17:4(135).

Blocken, B., Careliet, J. and Poesen, J. (2005), "Numerical simulation of the wind-driven rainfall distribution over small-scale topography in space and time", *J. Hydrology*, **315**(1-4), 252-273. https://doi.org/10.1016/j.jhydrol.2005.03.029.

Bruno, L., Horvat, M. and Raffaele, L. (2018), "Windblown sand along railway infrastructures: A review of challenges and mitigation measures", *J. Wind Eng. Ind., Aerod.*, **177**, 340-365. https://doi.org/10.1016/j.jweia.2018.04.021.

Cao, S. and Tamura, T. (2006), "Experimental study on roughness effects on turbulent boundary layer flow over a two-dimensional steep hill", *J. Wind Eng. Ind. Aerod.*, **94**, 1-19. https://doi.org/10.1016/j.jweia.2005.10.001.

Cao, S. and Tamura, T. (2007), "Effects of roughness blocks on atmospheric boundary layer flow over a two-dimensional low hill with/without sudden roughness change", *J. Wind Eng. Ind. Aerod.*, **95**, 679695. https://doi.org/10.1016/j.jweia.2007.01.002.

Claudin, P., Wiggs, G.F.S. and Andreotti, B. (2013), "Field evidence for the upwind velocity shift at the crest of low dunes", *Bound. Layer Meteorol.*, **148**, 195206. https://doi.org/10.1007/s10546-013-9804-3.

Comola, F., Giometto, M.G., Salesky, S.T., Parlange, M.B. and Lehning, M. (2019), "Preferential deposition of snow and dust over hills: Governing processes and relevant scales", *J. Geophysic. Res. Atmos.*, **124**, 79517974. https://doi.org/10.1029/2018JD029614.

Creyssels, M., Dupont, P., El Moctar, A.O., Valence, A., Cantat, I., Jenkins, J.T., Pasini, J.M. and Rasmussen, K.R. (2009), "Saltating particles in a turbulent boundary layer: experiment and theory", *J. Fluid Mech.*, **625**, 47-74. https://doi.org/10.1017/S0022112008005491.

Dong, Z., Wang, H., Liu, X. and Wang, X. (2004), "The blown sand flux over a sandy surface: a wind tunnel investigation on the fetch effect", *Geomorphology*, **57**(1-2), 117-127. https://doi.org/10.1016/S0169-555X(03)00087-4.

Essel, E.E., Nematollahi, A., Thacher, E.W. and Tachie, M.F. (2015), "Effects of upstream roughness and Reynolds number on separated and reattached turbulent flow", *J. Turbulence*, **16**(9), 872-899. https://doi.org/10.1080/14685248.2015.1033060.

Farimani, A.B., Ferreira, A.D. and Sousa, A.C.M. (2011), "Computational modeling of the wind erosion on a sinusoidal pile using a moving boundary method", *Geomorphology*, **130**(3-4), 299-311. https://doi.org/10.1016/j.geomorph.2011.04.012.

Ferreira, A.D. and Fino, M.R.M. (2012), "A wind tunnel study of wind erosion and profile reshaping of transverse sand piles in tandem", *Geomorphology*, **139-140**, 230-241. https://doi.org/10.1016/j.geomorph.2011.10.024.

Ferreira, A.D. Lopes, A.M.G., Viegas, D.X. and Sousa, A.C.M. (1995), "Experimental and numerical simulation of flow around two-dimensional hills", *J. Wind Eng. Indust. Aerodynamics*, **54-55**, 173-181. https://doi.org/10.1016/0167-6105(94)00040-K

Finnigan, J.J. (1988), *Air Flow Over Complex Terrain*, Springer, Berlin, Heidelberg. https://doi.org/10.1007/978-3-642-73845-6 13.

Goossens, D. (2006), "Aeolian deposition of dust over hills: the effect of dust grain size on the deposition pattern", *Earth Surface Processes and Landforms*, **31**, 762-776. https://doi.org/10.1002/esp.1272.

Ho, T.D., Valance, A., Dupont, P. and El Moctar, A.O. (2011), "Scaling Laws in Aeolian Sand Transport", *Phys. Rev. Lett.*, **106**(9), 094501. https://doi.org/10.1103/PhysRevLett.106.094501.

Hotta, S. and Horikawa, K. (1991), "Function of sand fence placed in front of embankment", *Coastal Eng.*, **2**, 2754-2767. https://doi.org/10.1061/9780872627765.211.

Huang, G., Le Ribault, C., Vinkovic, I. and Simoëns, S. (2019),

"Large-Eddy Simulation of erosion and deposition over multiple two-dimensional Gaussian hills in a turbulent boundary layer", *Bound. Layer Meteorol.*, **173**, 193-222. https://doi.org/10.1007/s10546-019-00463-2.

Ke, S., Dong, Y., Zhu, R. and Wang, T. (2020), "Wind-sand coupling movement induced by strong typhoon and its influences on aerodynamic force distribution of the wind turbine", *Wind Struct.*, **30**(4), 433-450. https://doi.org/10.12989/was.2020.30.4.433.

Kok, J.F., Parteli, E.J.R., Michaels, T.I. and Karam, D.B. (2012), "The physics of wind-blown sand and dust", *Reports Progress Phys.*, **75**(10), 106901. https://doi.org/10.1088/0034-4885/75/10/106901.

Lee, S.J., Lim, H.C. and Park, K.C. (2002), "Wind flow over sinusoidal hilly obstacles located in a uniform flow", *Wind Struct.*, **5**(6), 515-526. https://doi.org/10.12989/was.2002.5.6.515.

Lo Giudice, A., Nuca, R., Preziosi, L. and Coste, N. (2019), "Wind-blown particulate transport: A review of computational fluid dynamics models", *Mathem. Eng.*, **1**, 508-547. https://doi.org/10.3934/mine.2019.3.508.

Lo Giudice, A. and Preziosi, L. (2020), "A fully Eulerian multiphase model of windblown sand coupled with morphodynamic evolution: Erosion, transport, deposition, and avalanching", *Appl. Mathem. Model.*, **79**, 68-84. https://doi.org/10.1016/j.apm.2019.07.060.

Ma, W. and Li, F. and Sun, Y. and Li, J. and Zhou, X. (2021), "Field measurement and numerical simulation of snow deposition on an embankment in snowdrift", *Wind. Struct.*, **32**, 453-469. https://doi.org/10.12989/was.2021.32.5.453.

Martin, R.L. and Kok, J.F. (2017), "Wind-invariant saltation heights imply linear scaling of aeolian saltation flux with shear stress", *Sci. Adv.*, **3**, e1602569. https://doi.org/10.1126/sciadv.1602569.

Martínez, M.L., Hesp, P.A. and Gallego-Fernndez, J.B. (2013), *Coastal Dunes: Human Impact and Need for Restoration*, Springer. http://doi.org/10.1007/978-3-642-33445-0 1.

Parker, S.T. and Kinnersley, R.P. (2004), "A computational and wind tunnel study of particle dry deposition in complex topography", *Atmosp. Environ.*, **38**, 3867-3878. https://doi.org/10.1016/j.atmosenv.2004.03.046.

Phillips, D.A. (2011), "Analysis of Potential Sand Dune Impacts on Railway Tracks and Methods of Mitigation", *GCC Transport and Railway Conference*, 17-19, Doha, Qatar, http://www.iktissadevents.com/files/events/gtrc/1/presentations/d2-s8-duncan-phillips.pdf.

Porté -Agel, F., Bastankhah, M. and Shamsoddin, S. (2020), "Wind-Turbine and Wind-Farm Flows: A Review", *Bound. Layer Meteorol.*, **174**, 1-59. https://doi.org/10.1007/s10546-019-00473-0.

Preziosi, L., Fransos, D. and Bruno, L. (2015), "A multiphase first order model for non-equilibrium sand erosion, transport and sedimentation", *Appl Mathem. Lett.*, **45**, 69-75. https://doi.org/10.1016/j.aml.2015.01.011.

Raffaele, L. and Bruno, L. (2019), "Windblown sand action on civil structures: Definition and probabilistic modelling", *Eng. Struct.*, **178**, 88-101. https://doi.org/10.1016/j.engstruct.2018.10.017.

Raffaele, L. and Bruno, L. (2020), "Windblown sand mitigation along railway megaprojects: A comparative study", *Struct. Eng. Int.*, **30**, 355-364. https://doi.org/10.1080/10168664.2020.1714530.

Raffaele, L., Bruno, L., Pellerey, F. and Preziosi, L. (2016), "Windblown sand saltation: A statistical approach to fluid threshold shear velocity", *Aeolian Res.*, **23**, 79-91. https://doi.org/10.1016/j.aeolia. 2016.10.002.

Raffaele, L., Bruno, L. and Sherman, D.J. (2020), "Statistical characterization of sedimentation velocity of natural particles", *Aeolian Res.*, **44**, 100593. https://doi.org/10.1016/j.aeolia.2020.100593

Raffaele, L., Coste, N. and Glabeke, G. (2022), "Life-cycle performance and cost analysis of sand mitigation measures: Toward a hybrid experimental-computational approach", *J. Struct. Eng.*, **148**(7), 04022082. https://doi.org/10.1061/(ASCE)ST.1943-541X.0003344.

Raffaele, L., van Beeck, J. and Bruno, L. (2021), "Wind-sand tunnel testing of surface-mounted obstacles: Similarity requirements and a case study on a Sand Mitigation Measure", *J. Wind Eng. Indust. Aerodynamics*, **214**, 104653. https://doi.org/10.1016/j.jweia.2021.104653.

Safaei Pirooz, A.A. and Flay, R.G.J. (2017), "Comparison of speed-up over hills derived from wind-tunnel experiments, wind-loading standards, and numerical modelling", *Bound. Layer Meteorol.*, **168**, 213-246. https://doi.org/10.1007/s10546-018-0350-x.

Shao, Y. (2008), *Physics and Modelling of Wind Erosion*, Springer. https://doi.org/10.1007/978-1-4020-8895-7.

Sherman, D.J. (2020), "Understanding wind-blown sand: Six vexations", *Geomorphology*, **366**, 107193. https://doi.org/10.1016/j.geomorph.2020.107193.

Sherman, D.J. and Farrell, E.J. (2008), "Aerodynamic roughness lengths over movable beds: Comparison of wind tunnel and field data", *J. Geophysical Res. Earth Surf.*, **113**, F02S08. https://doi.org/10.1029/2007JF000784.

Sherman, D.J. and Nordstrom, K.F. (1994), "Hazards of wind-blown sand and coastal sand drifts: A review", *J. Coastal Res.*, **12**, 263-275.

Sherman, D.J., Zhang, P., Martin, R.L., Ellis, J.T., Kok, J.F., Farrell, E.J. and Li, B. (2019), "Aeolian ripple migration and associated creep transport rates", *Geosci.*, **9**(9), 389. https://doi.org/10.3390/geosciences9090389.

Simoëns, S., Saleh, A., Leribault, C., Belhmadi, M., Zegadi, R., Allag, F., Vignon, J.M. and Huang, G. (2015), "Influence of Gaussian Hill on concentration of solid particles in suspension inside turbulent boundary layer", *Procedia IUTAM*, **17**, 110-118. https://doi.org/10.1016/j.piutam.2015.06.015.

Snyder, W.H. and Castro, I.P. (2002), "The critical Reynolds number for rough-wall boundary layers", *J. Wind Eng. Indust. Aerodynamics*, **90**, 41-54. https://doi.org/10.1016/S0167-6105(01)00114-3.

Strypsteen, G., De Sloover, L., De Wulf, A. and Rauwoens, P. (2020), "Downwind evolution of aeolian saltation across an artificially constructed coastal berm", *Aeolian Res.*, **47**, 100627. https://doi.org/10.1016/j.aeolia.2020.100627.

Sun, L., Nottrott, A. and Kleissl, J. (2012), "Effect of hilly urban morphology on dispersion in the urban boundary layer", *Build. Env.*, **48**, 195-205. https://doi.org/10.1016/j.buildenv.2011.09.005.

Tominaga, Y., Okaze, T. and Mochida, A. (2018), "Wind tunnel experiment and CFD analysis of sand erosion/deposition due to wind around an obstacle", *J. Wind Eng. Ind. Aerod.*, **182**, 262-271. https://doi.org/10.1016/j.jweia.2018.09.008.

Valance, A., Rasmussen, K.R., Ould El Moctar, A. and Dupont, P. (2015), "The physics of Aeolian sand transport", *Comptes Rendus Physique*, **16**(1), 105-117. https://doi.org/10.1016/j.crhy.2015.01.006.

von Kármán, T. (1948), "Progress in the statistical theory of turbulence", *Proceed. Natl. Acad. Sci.*, **34**(11), 530-539. https://doi.org/10.1073/pnas.34.11.53.

White, B.R. (1996), "Laboratory simulation of aeolian sand transport and physical modeling of flow around dunes", *Annals Arid Zone*, **35**, 187-213.

Yu, Z., Zhu, F., Cao, R., Chen, X., Zhao, L. and Zhao, S. (2019), "Wind tunnel tests and CFD simulations for snow redistribution

on 3D stepped flat roofs", *Wind Struct*., **28**(1), 31-47. https://doi.org/10.12989/was.2019.28.1.031.

Zhang, N., Kang, J.H. and Lee, S.J. (2010), "Wind tunnel observation on the effect of a porous wind fence on shelter of saltating sand particles", *Geomorphology*, **120**, 224-232. https://doi.org/10.1016/j. geomorph.2010.03.032.

Zhou, X., Hu, J. and Gu, M. (2014), "Wind tunnel test of snow loads on a stepped flat roof using different granular materials", *Natural Hazards*, **74**, 1629-1648. https://doi.org/10.1007/s11069-014-1296-z.

AD